Dalton Transactions

ROYAL SOCIETY OF CHEMISTRY

PAPER

View Article Online
View Journal | View Issue

Cite this: *Dalton Trans.*, 2023, **52**, 5234

Improvement of carbon dioxide electroreduction by crystal surface modification of ZIF-8†

Ting Zhang,‡[a,b] Hong Liu, ‡[c,f] Xu Han,[a] Martí Biset-Peiró, [b] Yunhui Yang,[a] Inhar Imaz,[a] Daniel Maspoch, [a,d] Bo Yang, *[c] Joan Ramon Morante [b,e] and Jordi Arbiol *[a,d]

Received 19th January 2023,
Accepted 13th March 2023

DOI: 10.1039/d3dt00185g

rsc.li/dalton

Metal–organic frameworks (MOFs) possess high CO_2 adsorption properties and are considered to be a promising candidate for the electrochemical carbon dioxide reduction reaction (eCO_2RR). However, their insufficient selectivity and current density constrain their further exploration in the eCO_2RR. In this work, by introducing a very small proportion of 2,5-dihydroxyterephthalic acid (DOBDC) into ZIF-8, a surface modified ZIF-8-5% catalyst was synthesized by a post-modification method, exhibiting enhanced selectivity (from 56% to 79%) and current density (from –4 mA cm^{-2} to –10 mA m^{-2}) compared to ZIF-8. Density functional theory (DFT) calculations further demonstrate that the boosted eCO_2RR performance on ZIF-8-5% could be attributed to the improved formation of the *COOH intermediate stemming from successful DOBDC surface modification. This work opens a new path for improving the catalytic properties of MOFs *via* their surface modification.

1. Introduction

The electrochemical carbon dioxide reduction reaction (eCO_2RR) to obtain fuels and chemical feedstocks has been considered to be a promising option to mitigate the excessive emissions of CO_2 and to balance the global carbon cycle.[1–4] Among the various CO_2 RR products, carbon monoxide (CO) is one of the most promising and economically valuable candidates because it can be directly utilized as a feedstock for the preparation of value-added chemicals and complex multi-carbon products *via* the well-known Fischer–Tropsch synthesis.[5–9] Recently, metal–organic framework (MOF) materials have sparked considerable interest as novel catalysts in the field of eCO_2RR to produce CO, as both metal ions and organic ligands could influence the catalytic performance.[10–14] More importantly, the inherent porous confinement properties of MOFs are expected to induce a local CO_2 concentration enhancement, thus, facilitating eCO_2RR catalysis.[15,16] Despite these advantages, the current density for CO, when using pure MOF catalysts in the eCO_2RR, is still limited (usually lower than 3.4 mA cm^{-2}),[12] hindering the wide utilization of MOFs in electrocatalytic reactions.[14] Therefore, there is still a grand challenge to achieve MOF-based catalysts presenting high current densities while maintaining a high faradaic efficiency (FE), both properties being essentially required for practical applications.

Two key aspects should be primarily considered to achieve high eCO_2RR performance for a catalyst: (1) increasing the number of the exposed active sites and (2) promoting the mass transport of CO_2 or relevant species during the catalytic reaction.[14,17] To achieve these two goals, surface regulation of catalysts is reported as a promising method to simultaneously increase the number of exposed active sites and improve mass transport of the reactants.[18–20] For example, the number of active sites has been increased by the surface nitrogen-decoration strategy, leading to a high formate formation rate on surface decorated Sn.[21] Moreover, due to increased mass diffusion and transport, an enhanced FE of CO can be achieved on F-doped cage-like porous carbon through engineering the pore size distributions at the surface of a F-doped carbon shell.[17] Therefore, a rational chemical modification of the catalyst's surface could be an effective strategy to obtain a

[a]*Catalan Institute of Nanoscience and Nanotechnology (ICN2), CSIC and BIST, Campus UAB, Bellaterra, 08193 Barcelona, Catalonia, Spain. E-mail: arbiol@icrea.cat*
[b]*Catalonia Institute for Energy Research (IREC), Jardins de les Dones de Negre 1, Sant Adrià del Besòs, Barcelona 08930, Catalonia, Spain*
[c]*School of Physical Science and Technology, ShanghaiTech University, 393 Middle Huaxia Road, Shanghai 201210, China. E-mail: yangbo1@shanghaitech.edu.cn*
[d]*ICREA, Pg. Lluís Companys 23, 08010 Barcelona, Catalonia, Spain*
[e]*Department of Physics, Universitat de Barcelona, 08028 Barcelona, Catalonia, Spain*
[f]*State Key Laboratory of Information Functional Materials, 2020 X-Lab, ShangHai Institute of Microsystem and Information Technology, Chinese Academy of Sciences, Shanghai 200050, China.*

†Electronic supplementary information (ESI) available: SEM, TEM, EELS, XRD, Raman spectra, XPS, BET, gas calibration, *I–t*, LSV, and FE (H_2/CO), partial current densities of different samples, DFT results and ^{1}H-NMR results. See DOI: https://doi.org/10.1039/d3dt00185g

‡These authors contributed equally to this work.

high eCO_2RR performance, which would not largely change the crystal structure of the original bulk phase.[21] However, there are few reports on enhancing the eCO_2RR through regulating the surface of MOF catalysts. In particular, experimental and computational insights into such surface modification–performance relationship of MOF catalysts are still rare.

Here, we demonstrate that a surface modification strategy to treat ZIF-8 crystals with a polyphenolic acid such as 2,5-dihydroxyterephthalic acid (DOBDC) could bring about high-efficiency eCO_2RR performance. As an efficient etching and doping agent for MOFs, on the one hand, these acids can etch the surface of ZIF-8 crystals to create large surface areas and a high proportion of mesopores, potentially offering a large number of surface active sites for the eCO_2RR and allowing the facile diffusion of eCO_2RR-relevant species to the active sites.[22–24] On the other hand, DOBDC can adsorb onto the ZIF-8 surface, and then progressively replace partially the original organic linkers in ZIF-8 due to its ability to coordinate with metals,[25] thus, influencing the local environment of active sites to facilitate *COOH generation (the key intermediate for CO production).[13] Both experimental and theoretical results in this work reveal that this synergistic effect could promote the eCO_2RR performance on surface modified ZIF-8, realizing a dual improvement of selectivity and activity. In particular, through precisely controlling the DOBDC addition, when DOBDC is used at a concentration of 5% in weight with respect to ZIF-8 (hereafter denoted as ZIF-8-5%), ZIF-8-5% achieves a remarkable increase of the FE of CO up to 79% at −1.20 V *vs.* RHE, which is higher than that of the parent ZIF-8 (56%). More importantly, it also shows a 2.5 times higher CO current density, from −4 mA cm^{-2} on pure ZIF-8 to −10 mA cm^{-2} on ZIF-8-5%. Moreover, the selectivity can be retained over 60% in a range of working potentials from −1.0 to −1.2 V *vs.* RHE, proving that CO is still the main product on ZIF-8-5% at high overpotentials. Theoretical analyses further demonstrate that ZIF-8-5% could reduce the reaction energy for *COOH intermediate formation during the eCO_2RR process, thus enhancing the production efficiency of CO. We believe that this post-synthetic treatment could open a new way for boosting the catalytic performance of MOF-based catalysts with controllable surface modification.

2. Experimental section

2.1 Chemicals

If not specified, all chemical reagents were purchased from Sigma-Aldrich. Zinc nitrate hexahydrate ($Zn(NO_3)_2{\cdot}6H_2O$), 2-methylimidazole (2-mim), methanol, 2,5-dihydroxyterephthalic acid (DOBDC), *N*,*N*-dimethylformamide (DMF), ethanol and sodium bicarbonate ($NaHCO_3$) were all of analytical grade and used as received without further purification. Meanwhile, all solutions were prepared with Milli-Q water (DI-H_2O, Ricca Chemical, ASTM Type I). Nafion (N-117 membrane, 0.18 mm thick) was purchased from Alfa Aesar and kept in 0.5 M NaOH solution. Carbon paper was also purchased from Alfa Aesar.

2.2 Synthesis of ZIF-8

The fabrication of ZIF-8 was similar to the method in published reports.[13] Typically, 1.115 g of $Zn(NO_3)_2{\cdot}6H_2O$ was dissolved in 50 mL of methanol under magnetic stirring at room temperature to form a homogeneous solution. Then, 50 mL of methanolic solution containing 1.232 g of 2-mim were added into the above mixture solution under ultrasonication until a clear solution was formed. The obtained homogeneous solution reacted at room temperature for 24 h without stirring. Then, the white powder was collected by centrifugation, washed with methanol several times to remove the organic residual. The final products were then dried in a vacuum at 60 °C overnight.

2.3 Synthesis of Zn-MOF-74

The Zn-MOF-74 sample was synthesized according to previous published protocols with minor modification.[26,27] Firstly, 60 mg of $Zn(NO_3)_2{\cdot}6H_2O$ and 20 mg of DOBDC were dissolved in 15 mL of mixed DMF/H_2O/ethanol solution (v/v/v = 1 : 1 : 1) under ultrasonication to form a homogeneous solution. Then, the obtained solution was transferred into a Teflon reactor and heated at 120 °C for 24 h, then cooled to room temperature, brown crystals were obtained by centrifugation, and washed with DMF several times. Finally, the final products were dried in a vacuum at 60 °C overnight.

2.4 Synthesis of modified ZIF-8-*x* with the DOBDC modification

In this procedure, 300 mg of as-prepared ZIF-8 powder was dispersed in 45 mL of a mixture solution containing 15 mL of DMF, 15 ml of ethanol and 15 mL of water under ultrasound for 20 min at room temperature. After forming a homogeneous solution, DOBDC with different quantities (5 mg, 15 mg, 30 mg, 50 mg and 100 mg) was added into the above solution under ultrasound for 5 min at room temperature. The weights of DOBDC added correspond to 1.7%, 5%, 10%, 17% and 33% *vs.* the ZIF-8 weight, respectively. Next, the mixed solution was left in the oven at 60 °C for 7 days. After the reaction, the powders were collected by centrifugation, washed with ethanol and DMF several times and dried in a vacuum at 60 °C overnight. The samples have been labelled depending on the percentage of the added DOBDC: ZIF-8-1.7%, ZIF-8-5%, ZIF-8-10%, ZIF-8-17% and ZIF-8-33%, respectively.

2.5 Synthesis of a physical mixture of ZIF-8-5% (labelled as ZIF-8-5%-P)

For the preparation of the ZIF-8-5%-P sample, 15 mg of DOBDC powder were directly added into 300 mg of ZIF-8 powder and mixed well.

2.6 Preparation of working electrodes

10 mg of the different synthesized samples and 50 μl of 5 wt% Nafion solutions were dissolved in ethanol (1 mL) and ultrasonicated for 1 h to form even suspensions for further electrochemical experiments. To prepare the working electrode, 500 μL of the above as-prepared inks were dropped onto the

two sides of the carbon paper electrode with 1 × 1 cm^2 and then dried at room temperature for a few minutes, giving a catalyst total loading mass of ~2.5 mg cm^{-2}.

2.7 Electrochemical measurements and calculations

The electrocatalytic performance of different catalysts was measured at room temperature using a gas-tight H-cell with two-compartments separated by a Nafion N-117 membrane with a continuous Ar or CO_2 gas injection. Each compartment contained 70 mL of electrolyte (0.5 M $NaHCO_3$ made from deionized water). In a typical experiment, a standard three electrode setup in 0.5 M $NaHCO_3$ solution was assembled: an Ag/AgCl electrode was used as the reference electrode, a Pt sheet as the auxiliary electrode and carbon paper modified with the different samples as the working electrode (with a total surface area = 1 cm^2). The potentials were measured *versus* Ag/AgCl and converted to the reversible hydrogen electrode (RHE) according to the following equation: $E_{RHE} = E^{\circ}_{Ag/AgCl} + E_{Ag/AgCl} + 0.059 \times pH$, pH = 7.[28,29] All the electrochemical results are shown without iR-compensation and obtained using a computer-controlled BioLogic VMP3 electrochemical workstation.

Before the electrochemical CO_2 reduction experiments, an average rate of 20 mL min^{-1} Ar was injected to form an Ar-saturated solution. During electrochemical CO_2 reduction experiments, CO_2 gas was delivered at the same rate at room temperature and ambient pressure, measured downstream by a volumetric digital flowmeter. The gas phase composition was analyzed by gas chromatography (GC) during potentiostatic measurements every 20 min using a 490 Micro GC (Agilent Technologies). The calibration of peak area *vs.* gas concentration was used for the molar quantification of each gaseous effluent. The liquid products were analyzed afterwards by quantitative ^{1}H-NMR using water as the deuterated solvent. Moreover, the MOF sample was digested by HF solution overnight to completely destroy the structure. The ^{1}H-NMR of the sample was conducted using MeOD as the solvent.

Details of the calculation are shown below.

The partial current density for a given gas product was calculated as given below:[30]

$$j_i = x_i \times V \times \frac{n_i F P_0}{RT} \times (\text{electrode area})^{-1}$$

where x_i is the volume fraction of a certain product determined by online GC referenced to calibration curves from three standard gas samples, V is the flow rate, n_i is the number of electrons involved, P_0 = 101.3 kPa, F is the Faraday constant, T is temperature and R is the gas constant. The corresponding FE at each potential is calculated by

$$\text{FE} = \frac{j_i}{j} \times 100\%.$$

2.8 Characterization

X-ray diffraction patterns (XRD) were obtained using a Bruker D4 X-ray powder diffractometer using Cu Kα radiation (1.54184 Å). Field emission scanning electron microscopy (FE-SEM) images were collected on a FEI Magellan 400 L scanning electron microscope. Transmission electron microscopy (TEM) and high angle annular dark field scanning TEM (HAADF-STEM) images were obtained in a Tecnai F20 field emission gun microscope with a 0.19 nm point-to-point resolution at 200 kV equipped with an embedded Quantum Gatan image filter for EELS analyses. Images have been analyzed by means of the Gatan Digital Micrograph software. X-ray photoelectron spectroscopy (XPS) was performed on a Phoibos 150 analyzer (SPECS GmbH, Berlin, Germany) under ultra-high vacuum conditions (base pressure 4 × 10^{-10} mbar) with a monochromatic aluminum Kα X-ray source. Binding energies (BE) were determined using the C 1s peak at 284.5 eV as a charge reference. Raman spectra were obtained using Senterra. Brunauer–Emmett–Teller (BET) surface areas were measured using nitrogen adsorption at 77 K (TriStar II 3020-Micromeritics). Proton nuclear magnetic resonance (^{1}H-NMR) was conducted in a Bruker Advance III 400 MHz.

2.9 DFT calculations

DFT calculations were performed using the Vienna *ab initio* simulation package (VASP) code[31] with the projector augmented wave (PAW) method.[32–35] Generalized gradient approximation (GGA) with the Perdew–Burke–Ernzerhof (PBE) exchange–correlation function was used to set the plane wave basis.[36,37] The energy cutoff was 500 eV and all structures were allowed to relax. The force convergence criteria on each configuration were below 0.05 eV $Å^{-1}$. In order to avoid interactions between molecules in the periodic structures, we placed the model in a 20 Å × 20 Å × 20 Å cell. 1 × 1 × 1 *k*-point grids with the Monkhorst–Pack scheme were used for all systems. The DFT-D3 method with Becke–Jonson damping was utilised to include van der Waals interactions between molecules.[38,39]

Molecular orbital (MO) analyses were performed with the PBE function and dgdzvp2 basis sets in the Gaussian 09 program.[40] The ZIF-8 model was generated with four 2-mim ligands coordinating with the central Zn^{2+} to form a tetrahedral configuration, which is according to the approach reported previously.[13] The ZIF-8-5% structure was built with one DOBDC replacing two 2-mim of ZIF-8. The free energy of the reaction at each elementary step was estimated using the computational hydrogen electrode model,[41] and the following elementary steps were considered for the electrochemical CO_2RR to CO:

$$CO_2(g) + * + H^+(aq) + e^- \leftrightarrow COOH*$$

$$COOH* + H^+(aq) + e^- \leftrightarrow CO* + H_2O(l)$$

$$CO* \leftrightarrow CO(g) + *$$

where *, COOH* and CO* represent the free site and adsorption state of COOH and CO, respectively. The free energies of the reaction were calculated according to the following formula:

$$G = E_{DFT} + E_{ZPE} - TS + E_{sol}$$

where E_{DFT} is the DFT calculated total energy, E_{ZPE} represents the zero-point energy, and S is the entropy. E_{sol} is the solvation cor-

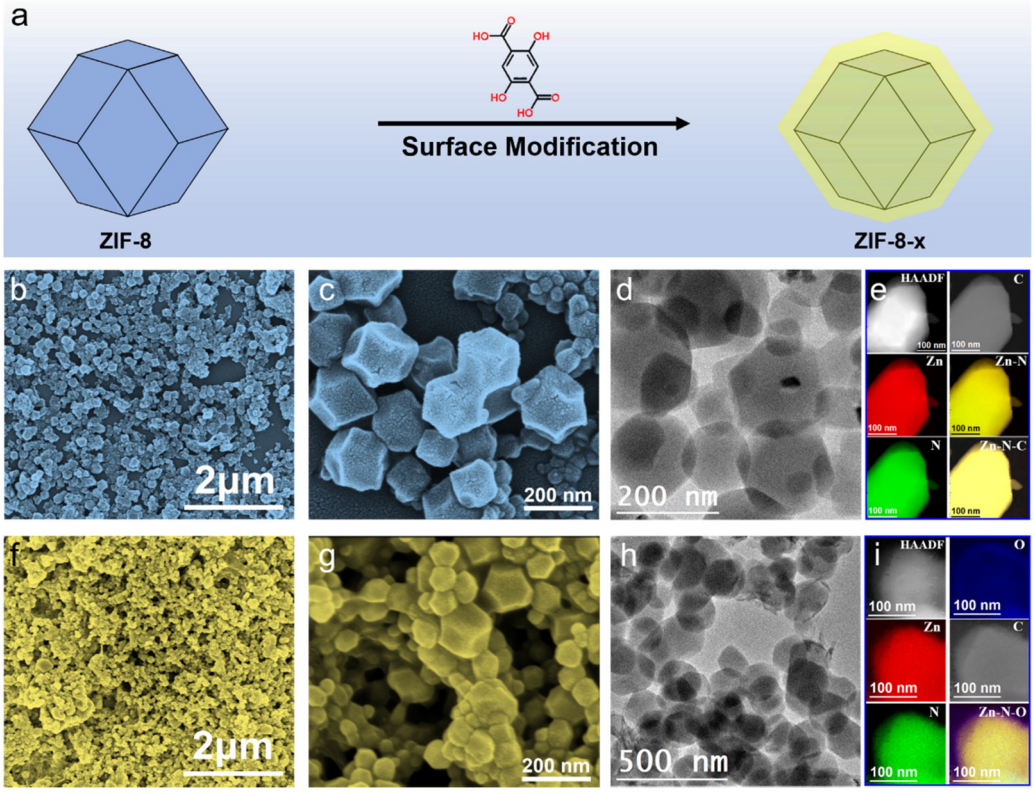

Fig. 1 (a) Schematic illustration of the formation of ZIF-8-*x* samples. (b and c) FE-SEM images, (d) BF TEM, (e) HAADF STEM and EELS chemical composition maps of ZIF-8. (f and g) FE-SEM images, (h) BF TEM, (i) HAADF STEM and EELS chemical composition maps of ZIF-8-5%. Individual Zn $L_{2,3}$-edges at 1020 eV (red), N K-edges at 401 eV (green), O K-edges at 532 eV (blue) and C K-edges at 285 eV (grey) as well as their composites.

rection and the values used for CO* was −0.1 eV and −0.25 eV for COOH*.[42]

3. Results and discussion

3.1 Structural characterization

A schematic illustration of the synthesis route followed to obtain the corresponding modified ZIF-8-*x* samples is shown in Fig. 1a. ZIF-8 is initially synthesized based on previous literature.[13] In a second step, the corresponding ZIF-8-*x* (where *x* represents the weight percentage of DOBDC with respect to ZIF-8) are prepared by incubating a dispersion of the pristine ZIF-8 crystals and different amounts of DOBDC in a mixture of DMF, ethanol and water. Following this synthetic protocol, five different samples denoted as ZIF-8-1.7%, ZIF-8-5%, ZIF-8-10%, ZIF-8-17% and ZIF-8-33% are prepared.

The surface morphology and elementary composition of the as-prepared samples are revealed by field emission scanning electron microscopy (FE-SEM) and transmission electron microscopy (TEM). As revealed by FE-SEM (Fig. 1b and c), the prepared ZIF-8 shows homogeneous crystals with the characteristic rhombic dodecahedral morphology. In addition, TEM analyses show that the ZIF-8 crystals have a size in the range of 80–200 nm (Fig. 1d). After DOBDC doping modification, various morphologies of ZIF-8-*x* samples are shown in Fig. 1f, g and Fig. S1.† As shown in Fig. S1a† and Fig. 1f, g, the as-synthesized ZIF-8-1.7% and ZIF-8-5% samples still inherit the original rhombic dodecahedral morphology, which is similar to the one shown by the pure ZIF-8 structures, suggesting that there is not an apparent morphology damage of these crystals after exposing them to a small proportion of DOBDC. With increasing ratios of DOBDC, the ZIF-8-10% sample displays an irregular spherical shape (Fig. S1b†), indicating the surface corrosion caused by the large concentration of DOBDC. However, ZIF-8-17% and ZIF-8-33% samples are composed by some larger bulks and small spherical particles. The formation of these bulky structures could be attributed to the coordination between excess DOBDC and liberated Zn(II) ions accompanied by further etching/dissolution of the sacrificial ZIF-8, forming other crystalline species. The chemical compositions of ZIF-8 and ZIF-8-5% crystals were further investigated by high angle annular dark filed scanning transmission electron microscopy (HAADF STEM) and electron energy loss spectroscopy (EELS) elemental maps. STEM EELS compositional maps show the homogeneous distribution of Zn, N and C in ZIF-8 and ZIF-8-5% crystals (Fig. 1e and i). It is worth noting that the presence of the element O in the ZIF-8-5% crystal indicates the successful doping DOBDC into ZIF-8.

These samples were further investigated by X-ray powder diffraction (XRD). Indeed, the XRD patterns of ZIF-8-1.7%, ZIF-8-5% and ZIF-8-10% suggest similar crystal patterns to that

of standard ZIF-8,[13] indicating that the addition of a low concentration (up to 10%) of DOBDC does not significantly change the crystal structure of ZIF-8 (Fig. 2a and Fig. S2†). However, the XRD patterns of ZIF-8-17% and ZIF-8-33% show the appearance of some additional diffraction peaks, demonstrating that introducing a high concentration of DOBDC could change the inner bulk phase of ZIF-8, which are in accordance with the results of SEM. To determine the surface area of different samples, Brunauer–Emmett–Teller (BET) measurements were performed. As shown in Fig. 2b, the measured surface area (1403 $m^2\ g^{-1}$) of ZIF-8 is fully consistent with the previously reported value.[43] Obviously, when DOBDC is introduced at a low concentration (up to 10%), all the modified ZIF-8-*x* show an increased surface area compared to the parent ZIF-8. In addition, the porosity of the ZIF-8 and ZIF-8-5% samples was investigated by N_2 adsorption–desorption measurement, as shown in Fig. S3.† Both ZIF-8 and ZIF-8-5% show a typical type I adsorption/desorption isotherm curve in Fig. S3a,† indicating that both samples have numerous micropores.[44,45] Notably, the existence of a higher proportion of mesopores observed on ZIF-8-5% (Fig. S3b†) could facilitate mass diffusion and transport of CO_2(aq) or the eCO_2RR-relevant species in solution.[17,24] The results proves that DOBDC can be used to tailor the surface of ZIF-8 to provide a large number of surface active sites for the eCO_2RR and enhance the mass diffusion.[46]

Furthermore, the chemical valence state and surface composition of the ZIF-8 and ZIF-8-5% samples have been proved by X-ray photoelectron spectroscopy (XPS). The full survey scan XPS spectrum shown in Fig. 2c indicates the presence of C, N, O and Zn in both ZIF-8 and ZIF-8-5% samples. Remarkably, the O signal in ZIF-8-5% is significantly larger than in ZIF-8. The high-resolution XPS spectra obtained on the Zn 2p shows two main peaks in both samples at around 1020 eV and 1044 eV (Fig. 2d), corresponding to Zn $2p_{3/2}$ and Zn $2p_{1/2}$, respectively, which indicates the presence of Zn^{2+} in both samples.[47] However, for the Zn 2p XPS spectrum of ZIF-8, a slight shift toward the low binding energy for the Zn $2p_{3/2}$ and Zn $2p_{1/2}$ peaks of ZIF-8-5% is ascribed to the introduced DOBDC ligand with electron-donating ability.[48] The N 1s spectra for ZIF-8 and ZIF-8-5% are shown in Fig. 2e, which reveals that both samples mainly show three major peaks corresponding to –NH–, Zn–N and –N═ at 398.0 eV, 399.2 eV and 400.3 eV, respectively.[13] The O 1s XPS core level spectra for ZIF-8-5% can be deconvoluted into three peaks at around at 532.8, 531.7 and 530.1 eV, which would be related to C–O, C═O and Zn–O, respectively (Fig. 2f).[49] These results support the successful introduction of DOBDC into the ZIF-8 crystal surface. In addition, as shown in Fig. S4,† red-shifts at *ca*. 643.5, 1147.2, 1188, 1461.5, 1503 and 1510.7 cm^{-1}, are observed in the high-resolution Raman peaks on ZIF-8 after surface modification by DOBDC doping. These shifts are attributed to the tiny torsion and stretching of the different bonds, revealing that the coordinated environment of ZIF-8 is influenced by the introduced DOBDC ligand.[50] Meanwhile, Fourier transform infrared spectrophotometry (FT-IR) of ZIF-8-5%, as shown in Fig. S5,† proves the formation of Zn–DOBDC coordination by the negligible peak from characteristic O–H vibration peaks in ZIF-8-5% compared to DOBDC.[25] Furthermore, successful introduction of DOBDC into ZIF-8 with a concentration of 5% has been directly investigated by ^{1}H-NMR. We digested the ZIF-8-5% sample and analysed the resulting solutions by ^{1}H-NMR. As shown in Fig. S6,† the ZIF-8-5% sample shows a small peak at 7.41 ppm attributed to the functional group of DOBDC, thus corroborating the successful introduction of DOBDC into ZIF-8-5%. We then calculated the DOBDC : 2-mim ratio for ZIF-8-5% by a comparison

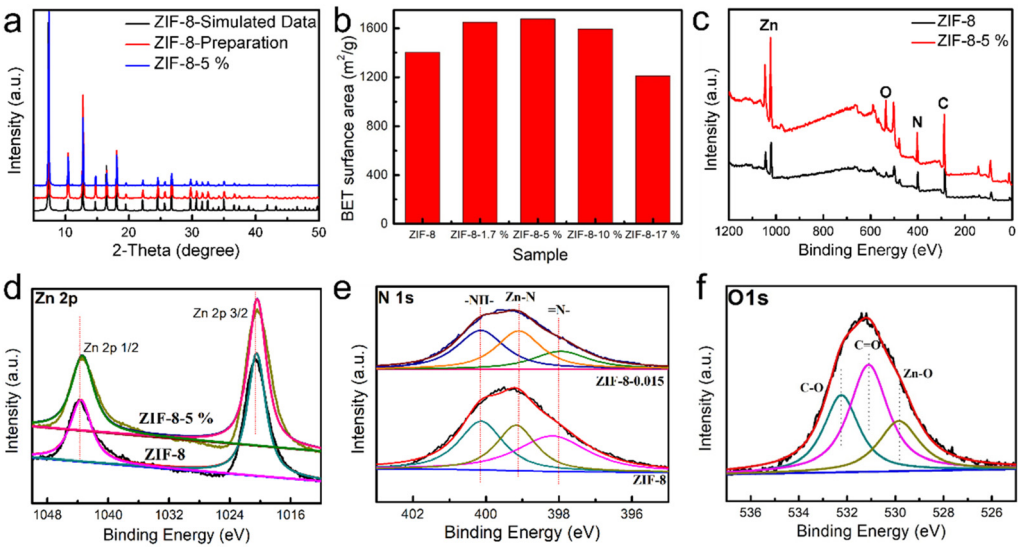

Fig. 2 (a) Simulated data from crystal structure and experimental XRD patterns of ZIF-8 and ZIF-8-5%. (b) The BET surface area of different samples. (c) XPS survey spectra, (d) high-resolution XPS spectra of Zn 2p, and (e) high resolution XPS spectra of N 1s on ZIF-8 and ZIF-8-5%. (f) High resolution XPS spectra of O 1s of ZIF-8-5%.

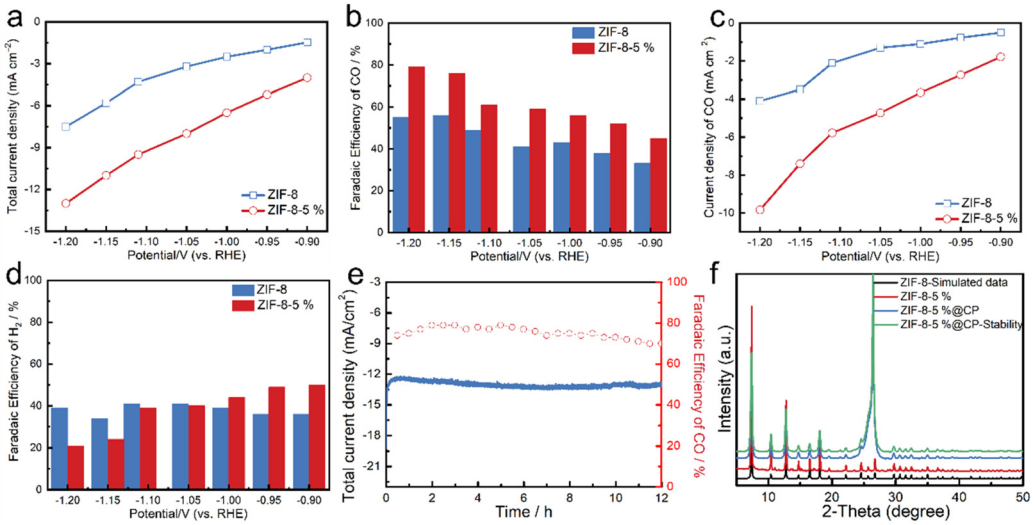

Fig. 3 (a) Total current densities, (b) corresponding FE for CO, (c) current densities of CO and (d) corresponding FE for H_2 on ZIF-8 and ZIF-8-5% coated on carbon paper in CO_2-saturated 0.5 M $NaHCO_3$ solution. (e) Current density *vs.* time (I–t) curve for ZIF-8-5% modified carbon paper at −1.20 V *vs.* RHE and (f) XRD pattern of ZIF-8-5% coated on the carbon paper before and after the stability test.

of the integration of the peak at 7.41 ppm corresponding to DOBDC and the peak at 7.17 ppm corresponding to 2-mim, indicating a DOBDC : 2-mim ratio of 0.02. All these results suggest that the surface modification with DOBDC was successful on ZIF-8-5%, which not only increases the surface area of the parent ZIF-8, but also successfully forms the Zn–DOBDC coordination.

3.2 eCO$_2$RR

The electrocatalytic activity of ZIF-8 and ZIF-8-5% coated on carbon paper with the same mass loading of 2.5 mg cm^{-2} was studied in Ar or CO_2-saturated 0.5 M $NaHCO_3$ solution as the electrolyte using a three-electrode H-cell. Before the eCO$_2$RR electrochemical tests, the prepared electrodes were pretreated at a constant potential of −0.90 V *vs.* RHE for 30 min until a stable current was reached (Fig. S7a and b†). To roughly evaluate the electroreduction ability of ZIF-8 and ZIF-8-5% samples, linear sweep voltammetry (LSV) curves under an Ar- and a CO_2-saturated atmosphere were obtained (Fig. S7c and d†). Under CO_2 purging, an enhanced current density could be observed on ZIF-8 and ZIF-8-5%, which was higher than that observed in an Ar-saturated solution, which confirmed the efficient catalytic performance of the ZIF-8 and ZIF-8-5% samples. Meanwhile, ZIF-8-5% shows a higher current density in CO_2-saturated solution than ZIF-8, delivering a higher activity toward the eCO$_2$RR. Fig. 3a shows the total current density plotted against the applied potential of both samples. The current density of the ZIF-8-5% sample increases to −13 mA cm^{-2} as the applied potential shifted negatively; however, a lower current density is observed at all applied potentials in the case of the ZIF-8 sample. The high current density achieved by ZIF-8-5% in comparison with that of the pristine ZIF-8 structure could be attributed to the increased active-site density caused by surface modification by DOBDC.[46,51] As shown in Fig. 3b, the parent ZIF-8 exhibits lower FE(CO) values similar to previous reports.[11] The FE(CO) for the ZIF-8-5% sample at each applied potential is higher than that of ZIF-8, with the highest FE(CO) of 79% at −1.20 V *vs.* RHE. In addition, according to Fig. 3c, the corresponding partial current densities of CO obtained on the ZIF-8-5% sample at all applied potentials are higher than those of ZIF-8, which reveals its higher reaction rate during the eCO$_2$RR.[7] Furthermore, the electrochemical active surface area (ECSA) was measured to confirm the high activity of ZIF-8-5%. It is established that an increase of the electrochemical active surface area often leads to the enhancement of catalytic activity.[28,52] The ECSA can be calculated by the electrochemical double-layer capacitance (C_{dl}) of active materials, which is generally proportional to their ECSA (ECSA = C_{dl}/C_s, C_s is specific capacitance). Therefore, the C_{dl} of ZIF-8 and ZIF-8-5% was probed by cyclic voltammogram (Fig. S8†). By plotting the $\Delta J = J_a - J_c$ against the scan rate, the slope which is twice of C_{dl} can be obtained. As shown in Fig. S8c,† the C_{dl} of surface modified ZIF-8-5% is significantly larger than that of ZIF-8, indicating that ZIF-8-5% could provide more active sites to contact with the reactant to accelerate the electrocatalytic CO_2 RR.[52] The operating stability of a catalyst is a significant parameter for its practical applications. In this manner, as displayed in Fig. 3e, the I–t curve for ZIF-8-5% is obtained, showing a negligible decay of the current density (from −9.7 to −10 mA cm^{-2}) and the FE(CO) (from 79 to 70%) during continuous electrolysis under a CO_2-sturated solution at −1.20 V *vs.* RHE for 12 h, indicating good stability of the prepared ZIF-8-5%, which was further confirmed by XRD measurement before and after the I–t test (Fig. 3f), in which no appreciable difference in the crystal structure was observed after 12 h of stability test in 0.5 M $NaHCO_3$, proving that the main structure of ZIF-8-5% had been retained. Meanwhile, ^{1}H-NMR analyses are performed to

detect the absence of any liquid byproducts after the stability measurement, revealing that there is no liquid byproduct produced during the CO_2 RR process (Fig. S9†). The above results strongly support that after the rational surface modification using DOBDC ZIF-8-5% could achieve both high current density and FE(CO) at high applied potentials.

The FE for CO and H_2 on different ZIF-8-*x* samples are shown in Fig. S10† for comparison. Apparently, other samples show lower FE(CO) than that of ZIF-8-5%. Such decreased selectivity is attributed to the concentration of DOBDC introduced. The FE (CO and H_2) values of ZIF-8-1.7% at applied potentials are similar to that of ZIF-8 (Fig. S11†), although this sample shows an increased surface area compared to that of ZIF-8. In order to reveal this phenomenon, we also digested ZIF-8-1.7% and analysed the resulting solutions by ^{1}H-NMR, as shown in Fig. S12.† There is no signal from the functional group of DOBDC observed in the ZIF-8-1.7% sample. Therefore, its FE(CO) is limited by deficient DOBDC content, leading to only the etching process occurring on the surface of ZIF-8-1.7%, while there is negligible Zn–DOBDC coordination formation because of deficient DOBDC content. However, for ratios above 17%, the significant decrease in their catalytic activities is due to the new crystalline species formed which tend to cover up the active sites and even further change the active sites of catalysts, as found in our SEM and XRD results. In addition, we further investigated the FE(CO) of a ZIF-8-5%-P sample prepared by a physical mixture of ZIF-8 and DOBDC. As observed in Fig. S13a,† the ZIF-8-5%-P shows poor CO selectivity, lower than 40% FE(CO) at all applied potentials. Therefore, we conclude that the enhanced eCO_2RR activity on ZIF-8-5% is mainly influenced by the rational DOBDC surface modification, which changes the coordinated environment of ZIF-8, thus, boosting the catalytic performance.

DFT calculations were performed to reveal the origin of the excellent activity obtained on ZIF-8-5% upon rational DOBDC surface modification. The catalyst models of ZIF-8 and ZIF-8-5% used in the simulations are shown in Fig. 4a–d, and the optimal adsorption configurations of reaction intermediates are presented in Fig. S14 and 15.† The Gibbs free energy profiles of CO_2 reduction to CO at 0 V and −1.0 V *vs.* RHE are shown in Fig. 4e and f. As indicated in these two profiles, CO_2 activation to form COOH* is endergonic at 0 V *vs.* RHE on the two catalysts studied while the subsequent steps of CO formation and desorption are exergonic. Therefore, COOH* formation is the potential-limiting reaction step in the electrocatalytic reduction of CO_2. In addition, the Gibbs energy of the COOH* formation reaction of ZIF-8 is 0.4 eV more positive than that of ZIF-8-5% at both 0 V and −1.0 V *vs.* RHE, strongly suggesting that ZIF-8-5% is much more active than ZIF-8 towards electrocatalytic reduction of CO_2 to CO, which is in good agreement with the experimental results shown in the current work.

Further molecular orbital (MO) analysis is performed to elucidate the origin of distinct behaviors of ZIF-8 and ZIF-8-5% for the formation of COOH*. The HOMO and LUMO energy levels of ZIF-8 and ZIF-8-5% are shown in Fig. 4g. Interestingly, ZIF-8 and ZIF-8-5% exhibit a similar level of HOMO energy. The difference lies in the LUMO energy wherein ZIF-8-5% shows a much lower LUMO energy (−3.90 eV) than ZIF-8 (−0.50 eV), forming a narrower HOMO–LUMO energy gap for ZIF-8-5%. It is well established that a narrow HOMO–LUMO energy gap is beneficial for the charge transfer process, thus making electrocatalytic CO_2 RR more efficient as observed in recent works.[53–55]

Moreover, in order to further confirm that the increase of catalytic activity comes from the *in situ* DOBDC doping modification instead of the formation of new crystals of Zn-MOF-74 assembled by DOBDC and liberating Zn^{2+} on the ZIF-8 surface, a pure Zn-MOF-74 sample was prepared using the DOBDC ligand and Zn^{2+} salts (Fig. S16†). Zn–MOF-74 was also tested for the eCO_2RR and exhibited poor performance for generating CO (below 20%) at each applied potential (Fig. S17†). In addition, a control experiment was performed to verify that the obtained CO comes from the reduction of CO_2 on ZIF-8-5%, instead of the DOBDC ligand decomposition, as shown in Fig. S18.†

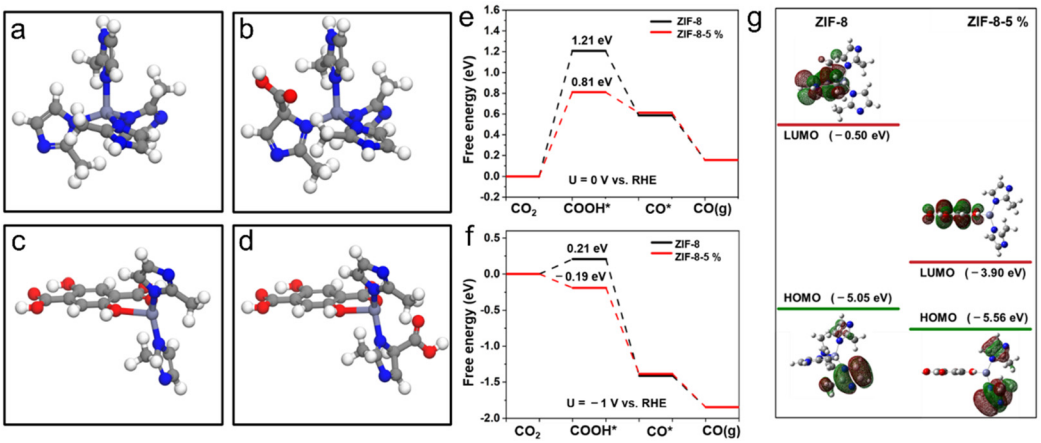

Fig. 4 The clean surface and optimized adsorption configuration on (a and b) ZIF-8 and (c and d) ZIF-8-5% surface model. (e and f) Free energy profiles for CO_2RR over ZIF-8 and ZIF-8-5% at 0 V and −1.0 V *vs.* RHE; (g) the HOMO and LUMO energy level of ZIF-8 and ZIF-8-5% models (Zn, C, N, O atoms are represented in purple, grey, blue, and red, respectively).

4. Conclusions

In summary, we systematically explored the surface modification strategy of ZIF-8 with DOBDC and found that it indeed influences the activity and selectivity towards CO production. In the case of the optimized ZIF-8-5% sample, an increase of selectivity towards the CO_2 RR is observed. The product selectivity to CO increased to 79%, which is higher than that of pristine ZIF-8 (56%). In addition, ZIF-8-5% also exhibited an enhanced CO partial current density of −10 mA cm^{-2} at −1.20 V *vs.* RHE, leading to a boosted CO production rate. The DFT calculations suggest that DOBDC modification not only maintains the active sites of ZIF-8 but also promotes the formation of COOH* during the eCO_2RR in the newly synthesized ZIF-8-5%. The enhanced ZIF-8-5% performance can be attributed to a decrease of the energy gap between the HOMO and LUMO. These results offer an efficient strategy to synthesize improved MOF-based materials towards CO_2 electroreduction by surface modification.

Conflicts of interest

There are no conflicts to declare.

Acknowledgements

The authors acknowledge funding from Generalitat de Catalunya 2021 SGR 01581 and 2021 SGR 00457. T. Z., J. R. M. and J. A. acknowledge funding from the projects (PID2020-116093RB-C42 and -C43) funded by MCIN/AEI/10.13039/501100011033 and by "ERDF A way of making Europe", by the "European Union". This study was supported by MCIN with funding from European Union NextGenerationEU (PRTR-C17.I1) and Generalitat de Catalunya. ICN2 is supported by the Severo Ochoa program from Spanish MCIN/AEI (grant no.: CEX2021-001214-S). ICN2 and IREC are funded by the CERCA Programme/Generalitat de Catalunya. A part of the present work has been performed in the framework of Universitat Autònoma de Barcelona Materials Science PhD program. T. Z. has received funding from the CSC-UAB PhD scholarship program (201706180028). X. H. and Y. H. Y. thank China Scholarship Council for scholarship support (201804910551 and 201806650010). Thanks to Guillaume Sauthier who carried out the XPS spectrum tests.

References

1 Y. J. Sa, C. W. Lee, S. Y. Lee, J. Na, U. Lee and Y. J. Hwang, *Chem. Soc. Rev.*, 2020, **49**, 6632–6665.
2 W. Shan, R. Liu, H. Zhao, Z. He, Y. Lai, S. Li, G. He and J. Liu, *ACS Nano*, 2020, **14**, 11363–11372.
3 A. Ozden, Y. Wang, F. Li, M. Luo, J. Sisler, A. Thevenon, A. Rosas-Hernández, T. Burdyny, Y. Lum, H. Yadegari, T. Agapie, J. C. Peters, E. H. Sargent and D. Sinton, *Joule*, 2021, **5**, 706–719.
4 T. Zhang, X. Han, H. Liu, M. Biset-Peiró, X. Zhang, P. Tan, P. Tang, B. Yang, L. Zheng, J. R. Morante and J. Arbiol, *Energy Environ. Sci.*, 2021, **14**, 4847–4857.
5 D. M. Koshy, S. Chen, D. U. Lee, M. B. Stevens, A. M. Abdellah, S. M. Dull, G. Chen, D. Nordlund, A. Gallo, C. Hahn, D. C. Higgins, Z. Bao and T. F. Jaramillo, *Angew. Chem., Int. Ed.*, 2020, **59**, 4043–4050.
6 Q. He, D. Liu, J. H. Lee, Y. Liu, Z. Xie, S. Hwang, S. Kattel, L. Song and J. G. Chen, *Angew. Chem., Int. Ed.*, 2020, **59**, 3033–3037.
7 O. S. Bushuyev, P. De Luna, C. T. Dinh, L. Tao, G. Saur, J. van de Lagemaat, S. O. Kelley and E. H. Sargent, *Joule*, 2018, **2**, 825–832.
8 X. Han, T. Zhang, M. Biset-Peiró, X. Zhang, J. Li, W. Tang, P. Tang, J. R. Morante and J. Arbiol, *ACS Appl. Mater. Interfaces*, 2022, **14**, 32157–32165.
9 T. Zhang, X. Han, H. Liu, M. Biset-Peiró, J. Li, X. Zhang, P. Tang, B. Yang, L. Zheng, J. R. Morante and J. Arbiol, *Adv. Funct. Mater.*, 2022, **32**, 2111446.
10 W. Geng, W. Chen, G. Li, X. Dong, Y. Song, W. Wei and Y. Sun, *ChemSusChem*, 2020, **13**, 4035–4040.
11 Y. Wang, P. Hou, Z. Wang and P. Kang, *ChemPhysChem*, 2017, **18**, 3142–3147.
12 X. Jiang, H. Li, J. Xiao, D. Gao, R. Si, F. Yang, Y. Li, G. Wang and X. Bao, *Nano Energy*, 2018, **52**, 345–350.
13 S. Dou, J. Song, S. Xi, Y. Du, J. Wang, Z.-F. Huang, Z. J. Xu and X. Wang, *Angew. Chem., Int. Ed.*, 2019, **58**, 4041–4045.
14 S. Dou, X. Li and X. Wang, *ACS Mater. Lett.*, 2020, **2**, 1251–1267.
15 D.-H. Nam, P. De Luna, A. Rosas-Hernández, A. Thevenon, F. Li, T. Agapie, J. C. Peters, O. Shekhah, M. Eddaoudi and E. H. Sargent, *Nat. Mater.*, 2020, **19**, 266–276.
16 C. S. Diercks, Y. Liu, K. E. Cordova and O. M. Yaghi, *Nat. Mater.*, 2018, **17**, 301–307.
17 W. Ni, Y. Xue, X. Zang, C. Li, H. Wang, Z. Yang and Y.-M. Yan, *ACS Nano*, 2020, **14**, 2014–2023.
18 P. Chen, Y. Tong, C. Wu and Y. Xie, *Acc. Chem. Res.*, 2018, **51**, 2857–2866.
19 L. Cao and C. Wang, *ACS Cent. Sci.*, 2020, **6**, 2149–2158.
20 L. Jiao, J. Wang and H.-L. Jiang, *Acc. Mater. Res.*, 2021, **2**, 327–333.
21 H. Cheng, S. Liu, J. Zhang, T. Zhou, N. Zhang, X.-s. Zheng, W. Chu, Z. Hu, C. Wu and Y. Xie, *Nano Lett.*, 2020, **20**, 6097–6103.
22 X. Song, Z. Ou, X. Hu, X. Zhang, M. Lin, L. Wen and M. Li, *ACS Mater. Lett.*, 2021, **3**, 171–178.
23 M. Hu, Y. Ju, K. Liang, T. Suma, J. Cui and F. Caruso, *Adv. Funct. Mater.*, 2016, **26**, 5827–5834.
24 Y. Liu, Z. Liu, N. Lu, E. Preiss, S. Poyraz, M. J. Kim and X. Zhang, *Chem. Commun.*, 2012, **48**, 2621–2623.
25 H. Wang, W. Zhu, Y. Ping, C. Wang, N. Gao, X. Yin, C. Gu, D. Ding, C. J. Brinker and G. Li, *ACS Appl. Mater. Interfaces*, 2017, **9**, 14258–14264.
26 X. Wang, H. Xiao, A. Li, Z. Li, S. Liu, Q. Zhang, Y. Gong, L. Zheng, Y. Zhu, C. Chen, D. Wang, Q. Peng, L. Gu, X. Han, J. Li and Y. Li, *J. Am. Chem. Soc.*, 2018, **140**, 15336–15341.

27 H. Q. Wu, L. Huang, J. Q. Li, A. M. Zheng, Y. Tao, L. X. Yang, W. H. Yin and F. Luo, *Inorg. Chem.*, 2018, **57**, 12444–12447.
28 T. Zhang, J. Du, P. Xi and C. Xu, *ACS Appl. Mater. Interfaces*, 2017, **9**, 362–370.
29 J. Yin, Q. Fan, Y. Li, F. Cheng, P. Zhou, P. Xi and S. Sun, *J. Am. Chem. Soc.*, 2016, **138**, 14546–14549.
30 T. Zheng, K. Jiang, N. Ta, Y. Hu, J. Zeng, J. Liu and H. Wang, *Joule*, 2019, **3**, 265–278.
31 J. Hafner, *J. Comput. Chem.*, 2008, **29**, 2044.
32 P. E. Blöchl, *Phys. Rev. B: Condens. Matter Mater. Phys.*, 1994, **50**, 17953–17979.
33 G. Kresse and J. Furthmüller, *Phys. Rev. B: Condens. Matter Mater. Phys.*, 1996, **54**, 11169–11186.
34 G. Kresse and J. Furthmüller, *Comput. Mater. Sci.*, 1996, **6**, 15–50.
35 G. Kresse and D. Joubert, *Phys. Rev. B: Condens. Matter Mater. Phys.*, 1999, **59**, 1758–1775.
36 J. P. Perdew, K. Burke and M. Ernzerhof, *Phys. Rev. Lett.*, 1996, **77**, 3865–3868.
37 J. P. Perdew, K. Burke and M. Ernzerhof, *Phys. Rev. Lett.*, 1997, **78**, 1396–1396.
38 S. Grimme, J. Antony, S. Ehrlich and H. Krieg, *J. Chem. Phys.*, 2010, **132**, 154104.
39 S. Grimme, S. Ehrlich and L. Goerigk, *J. Comput. Chem.*, 2011, **32**, 1456–1465.
40 N. Godbout, D. R. Salahub, J. Andzelm and E. Wimmer, *Can. J. Chem.*, 1992, **70**, 560–571.
41 J. K. Nørskov, J. Rossmeisl, A. Logadottir, L. Lindqvist, J. R. Kitchin, T. Bligaard and H. Jónsson, *J. Phys. Chem. B*, 2004, **108**, 17886–17892.
42 A. A. Peterson, F. Abild-Pedersen, F. Studt, J. Rossmeisl and J. K. Nørskov, *Energy Environ. Sci.*, 2010, **3**, 1311–1315.
43 J. K. Zaręba, M. Nyk and M. Samoć, *Cryst. Growth Des.*, 2016, **16**, 6419–6425.
44 C. Wang, Q. Lai, P. Xu, D. Zheng, X. Li and H. Zhang, *Adv. Mater.*, 2017, **29**, 1605815.
45 C. Chen, H. Huang, Y. Yu, J. Shi, C. He, R. Albilali and H. Pan, *Chem. Eng. J.*, 2018, **353**, 584–594.
46 C.-W. Kung, C. O. Audu, A. W. Peters, H. Noh, O. K. Farha and J. T. Hupp, *ACS Energy Lett.*, 2017, **2**, 2394–2401.
47 K. Liu, J. Wang, M. Shi, J. Yan and Q. Jiang, *Adv. Energy Mater.*, 2019, **9**, 1900276.
48 J. Liu, S. Zou, L. Xiao and J. Fan, *Catal. Sci. Technol.*, 2014, **4**, 441–446.
49 Z. Liu, Z. Zhao, Y. Wang, S. Dou, D. Yan, D. Liu, Z. Xia and S. Wang, *Adv. Mater.*, 2017, **29**, 1606207.
50 S. Tanaka, K. Fujita, Y. Miyake, M. Miyamoto, Y. Hasegawa, T. Makino, S. Van der Perre, J. Cousin Saint Remi, T. Van Assche, G. V. Baron and J. F. M. Denayer, *J. Phys. Chem. C*, 2015, **119**, 28430–28439.
51 N. Kornienko, Y. Zhao, C. S. Kley, C. Zhu, D. Kim, S. Lin, C. J. Chang, O. M. Yaghi and P. Yang, *J. Am. Chem. Soc.*, 2015, **137**, 14129–14135.
52 Z. Xin, Y.-R. Wang, Y. Chen, W.-L. Li, L.-Z. Dong and Y.-Q. Lan, *Nano Energy*, 2020, **67**, 104233.
53 Q. Wu, M.-J. Mao, Q.-J. Wu, J. Liang, Y.-B. Huang and R. Cao, *Small*, 2021, **17**, 2004933.
54 J. Zhu and S. Mu, *Adv. Funct. Mater.*, 2020, **30**, 2001097.
55 L. Sun, Z. Huang, V. Reddu, T. Su, A. C. Fisher and X. Wang, *Angew. Chem., Int. Ed.*, 2020, **59**, 17104–17109.